



# A family of low dispersive and low dissipative explicit schemes for flow and noise computations

Christophe Bogey \*, Christophe Bailly

*Laboratoire de Mécanique des Fluides et d'Acoustique, UMR CNRS 5509, Ecole Centrale de Lyon, 69134 Ecully, France*

Received 1 August 2002; received in revised form 5 May 2003; accepted 22 September 2003

---

## Abstract

Explicit numerical methods for spatial derivation, filtering and time integration are proposed. They are developed with the aim of computing flow and noise with high accuracy and fidelity. All the methods are constructed in the same way by minimizing the dispersion and the dissipation errors in the wavenumber space up to  $k\Delta x = \pi/2$  corresponding to four points per wavelength. They are shown to be more accurate, and also more efficient numerically, than most of the standard explicit high-order methods, for uniform and slowly non-uniform grids. Two problems involving long-range sound propagation are resolved to illustrate their respective precisions. Remarks about their practical applications are then made, especially about the connection with the boundary conditions. Finally, their relevance for the simulation of turbulent flows is emphasized.

© 2003 Elsevier B.V. All rights reserved.

AMS: 65C20; 76M20; 76Q05

Keywords: Explicit schemes; Low dispersion; Low dissipation; High-order; Finite differences; Selective filters; Low storage Runge–Kutta algorithms; Computational aeroacoustics; Large Eddy Simulation

---

## 1. Introduction

The need of highly accurate numerical methods was recognized from the earliest stages in the development of Computational AeroAcoustics [1]. The propagation of sound waves in far-field requires long-time integration with minimal dissipation and dispersion, and this cannot be done using the schemes generally used in Computational Fluid Dynamics. Therefore, new schemes with higher accuracy were proposed. The first ones were relative to the spatial derivation with finite-difference schemes showing dispersive properties optimized in the wavenumber space: among them, the explicit Dispersion-Relation-Preserving (DRP) [2], implicit compact [3–7], and ENO schemes [8]. The filtering which must be used to ensure numerical stability was then improved to decrease the dissipative effects on the resolved wavenumbers, and both explicit [9,10]

---

\* Corresponding author. Fax: 33-4-72-18-91-43.

E-mail address: [christophe.bogey@ec-lyon.fr](mailto:christophe.bogey@ec-lyon.fr) (C. Bogey).

and implicit selective filters [3,11] were provided. Finally, time integration was also optimized for noise computation, and low-dissipation and low-dispersion Adams–Bashforth [2] and Runge–Kutta algorithms [4,12–14] were formulated. The list just drawn above is not exhaustive, and other numerical methods were improved, such as the MacCormack schemes [15], for instance.

The present work is in keeping up with the more general pattern of computing noise directly from the unsteady compressible Navier–Stokes equations. This approach is very attractive, since both the flow and the sound field are intended to be calculated with a high precision by the same computation. In this way, not only the sound propagation but also the noise generation must be taken into account numerically, and the turbulent flow must be correctly described to provide the physical acoustic sources. Thus, the use of accurate schemes is crucial as much for the flow simulation as for the sound propagation itself. This issue is of great importance using the Large Eddy Simulation (LES) approach [16,17], where the turbulent scales are calculated up to the grid cut-off wavenumber, whereas effects of the unresolved scales are modeled [18]. In LES, the numerical algorithm must account for the spectral cut-off properly [19], by introducing negligible dissipation and dispersion on the resolved scales, and this requirement is still more acute with the modelings based on dynamic procedures [20] which evaluate the subgrid terms from the smaller resolved scales. It has been recently demonstrated that numerical errors can exceed the magnitude of the subgrid terms [21], and that a poor calculation of the smaller scales can significantly modify the contribution of these terms [22].

The motivation of the present work is to provide the numerical methods necessary for an explicit algorithm, following the requirements listed above. Schemes are developed in the same way as those specific to Computational AeroAcoustics. However, instead of demanding an accuracy limit for about seven points per wavelength such as the DRP scheme [2], the spatial-discretization methods must calculate the waves up to four points per wavelength with the aim of dynamic LES subgrid models. The time-integration methods must also have better stability properties than those found in the literature [4,12,13]. In the present work, central finite-difference schemes for spatial-derivation, selective filters for removing grid-to-grid oscillations, and low-storage Runge–Kutta algorithms for time advancement are optimized by minimizing their dispersion and dissipation errors for the same range of wavenumbers. Test filters with characteristics improved in the wavenumber space are also proposed for LES. Great attention is drawn to develop formulations with a high accuracy, but also with a high numerical efficiency to decrease their computational costs. Systematic comparisons with standard explicit methods are made, and two basic test problems are solved. The first one is a long-range propagation problem, and the second one is devoted to LES since waves with four points per wavelength are involved. The connection of the optimized schemes with boundary conditions and their properties for non-uniform grids are then discussed, and the issue of their applications for simulating turbulent flows, especially using LES, is addressed.

Optimized finite-difference schemes, selective filters, low-storage Runge–Kutta algorithms and test filters are presented in Sections 2–5 respectively. Dispersive and dissipative properties are shown, and both numerical accuracy and efficiency are reported. In Section 6, the test problems are solved using the optimized and standard methods. Informations on the practical applications of the optimized schemes are given in Section 7. Concluding remarks are drawn in Section 8. Finally, the coefficients of the schemes are provided in appendices A, B, C and D.

## 2. Finite-difference schemes for spatial derivation

The spatial derivative  $\partial u / \partial x$  at  $x_0$  can be approximated by a central,  $2N + 1$  point stencil, finite-difference scheme as

$$\frac{\partial u}{\partial x}(x_0) = \frac{1}{\Delta x} \sum_{j=-N}^N a_j u(x_0 + j\Delta x), \quad (1)$$

where  $\Delta x$  is the spacing of a uniform mesh, and the coefficients  $a_j$  are such as  $a_j = -a_{-j}$ , providing a scheme without dissipation. For standard schemes, the coefficients  $a_j$  are determined to cancel the terms of the Taylor series of (1) so that the maximum order is reached. Thus, the standard schemes using 9, 11 and 13 points, hereafter referred to as FDs9p, FDs11p and FDs13p, are of order 8, 10 and 12, respectively. Their coefficients are reported in Appendix A.

In this work, following Tam and Webb [2], schemes are constructed from their dispersion properties. By applying spatial Fourier transform to (1), the effective wavenumber  $k^*$  of the scheme is given by

$$k^* \Delta x = 2 \sum_{j=1}^N a_j \sin(jk \Delta x).$$

The dispersion error is the difference between the effective and the exact wavenumbers  $k^*$  and  $k$ . Finite-difference schemes using 9, 11 and 13 points, referred to as FDo9p, FDo11p and FDo13p, are developed so that the dispersion error is small for a large range of wavenumbers up to  $k \Delta x = \pi/2$ . They are of fourth order, and their coefficients  $a_j$  are defined to minimize the integral error

$$\int_{\ln(k \Delta x)_l}^{\ln(k \Delta x)_h} |k^* \Delta x - k \Delta x| d(\ln(k \Delta x)),$$

where the wavenumber limits are  $(k \Delta x)_l = \pi/16$ , and  $(k \Delta x)_h = \pi/2$  for FDo9p and FDo11p, but  $3\pi/5$  for FDo13p. The coefficients  $a_j$  thus determined are provided in Appendix A.

The relation between the effective and the exact wavenumbers for the optimized schemes is shown in Fig. 1 for  $0 < k \Delta x < \pi$ . The schemes are low dispersive as long as there is a good superposition with the line  $k^* \Delta x = k \Delta x$ . Increasing the number of points, from  $N = 3$  to 6, allows apparently to decrease the dispersion error for short waves. One must also note that the grid-to-grid waves with  $k \Delta x = \pi$  are never resolved.

The error between the effective and the exact wavenumbers,  $E_k(k \Delta x) = |k^* \Delta x - k \Delta x|/\pi$ , is represented in Figs. 2(a) and (b) for the standard and the optimized schemes, respectively, for  $\pi/8 \leq k \Delta x \leq \pi$  and in logarithmic scales. The optimized schemes are clearly less dispersive than the standard ones for short waves with  $k \Delta x > \pi/4$ . The reduction of the error is particularly important for the wavenumbers near  $k \Delta x = \pi/2$ , with at least one order of magnitude between the optimized and the standard schemes. The optimized schemes are also more dispersive for long waves because of their lower formal order, but the dispersion error is then very small, about or less than  $10^{-5}$ .

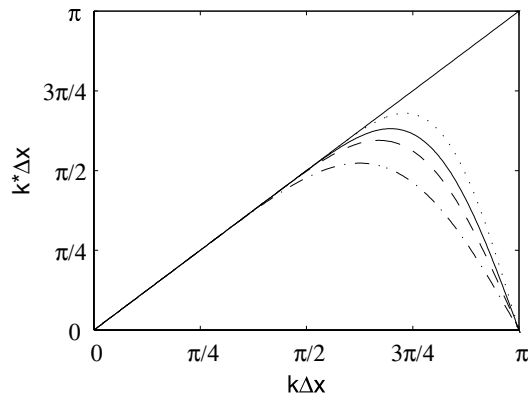


Fig. 1.  $k^* \Delta x$  versus  $k \Delta x$  for the optimized finite-difference schemes: ---, FDo9p ( $N = 4$ ); —, FDo11p ( $N = 5$ ); ····, FDo13p ( $N = 6$ ) and -·-·- for the DRP scheme of Tam and Webb [2] ( $N = 3$ ).

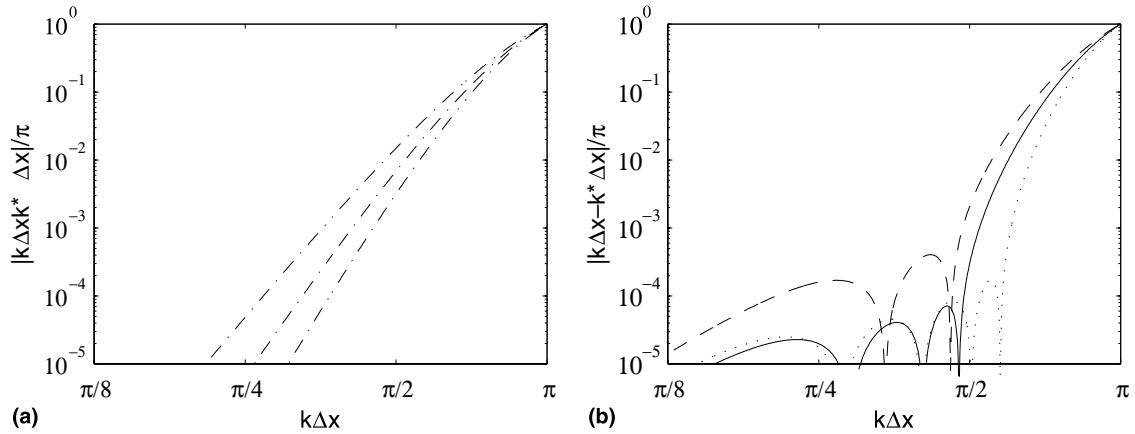


Fig. 2. Dispersion error, in logarithmic scales, for: (a) ----- the three standard schemes FDs9p, FDs11p and FDs13p; (b) the optimized schemes ---, FDo9p; —, FDo11p and ···· FDo13p.

To compare quantitatively the finite-difference schemes, two accuracy limits are estimated from the arbitrary criteria  $E_k \leq 5 \times 10^{-4}$  and  $E_k \leq 5 \times 10^{-5}$ . The first limit indicates the maximum wavenumber properly calculated and is expressed in term of number of points per wavelength, by  $\lambda_p/\Delta x$ . The second one indicates the maximum wavenumber accurately calculated and is given by  $\lambda_a/\Delta x$ . They are reported in Table 1 for the standard and the optimized schemes. For the same  $2N + 1$  stencil, the optimized schemes have generally better accuracy limits than the standard ones. Furthermore, waves with about four points per wavelength are taken into account only by FDo11p and FDo13p. Using these two optimized schemes, even the short waves are calculated very accurately since  $\lambda_a/\Delta x \simeq 4.6$ .

The numerical efficiency is now investigated through the product of the accuracy limits by the number of points  $2N + 1$ . This quantity, corresponding to a ratio between computational cost and accuracy, must be small. Values for the standard and the optimized schemes are given in Table 1. For the standard schemes, they are very similar showing that cost and accuracy vary proportionally. The optimized schemes, especially FDo11p and FDo13p, appear to be more efficient. For the same computational cost, they are more precise than any standard scheme.

Table 1

Accuracy limits of the standard and optimized FD schemes for  $N = 4, 5, 6$ ; and products by the number of points  $p = 2N + 1$  of the stencil

	$\lambda_p/\Delta x$	$\lambda_a/\Delta x$	$p\lambda_p/\Delta x$	$p\lambda_a/\Delta x$
FDs9p	6.09	7.97	54.8	71.4
FDs11p	5.25	6.58	57.7	72.4
FDs13p	4.72	5.75	61.4	74.7
FDo9p	4.22	11.84	38	106.6
FDo11p	3.93	4.65	43.2	51.2
FDo13p	3.36	4.66	43.7	60.6

For comparison, with the DRP scheme [10] for  $N = 3$ :  $\lambda_p/\Delta x = 5.8$  and  $\lambda_a/\Delta x = 13.1$ .

### 3. Selective filters

The grid-to-grid oscillations are not solved by central finite-difference schemes, as illustrated in Fig. 1, and must be removed because they can lead to numerical instabilities. Practically, the elimination of these spurious short waves is obtained by introducing artificial dissipation through additional damping terms in the equations [23] or, more efficiently, through filtering [11,24] without affecting the physical long waves.

Applying a central,  $2N + 1$  point stencil filter to variable  $u$  on a uniform mesh provides

$$u^f(x_0) = u(x_0) - \sigma_d D_u(x_0), \quad \text{with } D_u(x_0) = \sum_{j=-N}^N d_j u(x_0 + j\Delta x), \quad (2)$$

where the coefficients  $\overline{d_j}$  are such as  $d_j = d_{-j}$ , ensuring no dispersion, and  $\sigma_d$  is a constant between 0 and 1. The standard approach [19] for determining  $d_j$  consists in cancelling the terms resulting from the Taylor series of (2) for  $k\Delta x \rightarrow 0$ . In this way, the standard selective filters using 9, 11 and 13 points, referred to as SFs9p, SFs11p and SFs13p, are of order 8, 10 and 12, respectively. Their coefficients are reported in Appendix B.

To develop selective filters in the present work following the idea of Tam et al. [9,10], the spatial Fourier transform of (2) is considered,

$$D_k(k\Delta x) = d_0 + \sum_{j=1}^N 2d_j \cos(jk\Delta x), \quad (3)$$

where  $D_k(k\Delta x = 0) = 0$  and  $D_k(k\Delta x = \pi) = 1$  for normalization. This damping function  $D_k(k\Delta x)$  shows the amount of dissipation for any wavenumber. Filters SFo9p, SFo11p and SFo13p, on 9, 11 and 13 points, respectively, are built up by imposing small values to  $D_k(k\Delta x)$  in the range  $\pi/16 \leq k\Delta x \leq \pi/2$ . The filters SFo9p and SF13p are of fourth order and the filter SFo11p of second order, and their coefficients  $d_j$  are optimized to minimize the integral dissipation

$$\int_{\ln(\pi/16)}^{\ln(\pi/2)} D_k(k\Delta x) d(\ln(k\Delta x)).$$

Two conditions must also be met for  $0 < k\Delta x < \pi$ . The filters must exclusively be dissipative, implying  $D_k > 0$ , and to limit the variations of the damping function, we impose  $\partial \ln(D_k)/\partial \ln(k\Delta x) \geq -5$  for SFo9p and SFo11p, and  $\partial \ln(D_k)/\partial \ln(k\Delta x) \geq -10$  for SFo13p. The coefficients  $d_j$  thus determined are given in Appendix B.

The damping functions of the optimized filters are displayed in Fig. 3. As expected, the dissipation is small for long waves and is significant for the wavenumbers near  $k\Delta x = \pi$ . Increasing the number of points, from  $N = 3$  to 6, allows to construct more selective, spectral-like filters.

The damping functions of the standard and the optimized filters are represented in logarithmic scales in Figs. 4(a) and (b), for  $\pi/8 \leq k\Delta x \leq \pi$ . The optimized filters are less dissipative for short waves with about  $k\Delta x > \pi/4$ , the difference being considerable for  $k\Delta x$  close to  $\pi/2$ . Because of their second or fourth order, they are more dissipative for long waves but the amount of dissipation remains very small.

The two criteria  $\sigma_d D_k \leq 5 \times 10^{-4}$  and  $\sigma_d D_k \leq 5 \times 10^{-5}$  are now used to determine the wavenumbers dissipated by the selective filters in a small or in a negligible way, respectively. Since filtering is applied at every iteration, it is not necessary to set  $\sigma_d = 1$ , and values of  $\sigma_d$  between 0.1 and 0.2 are usually convenient for numerical stability. A value of  $\sigma_d = 0.2$  is chosen in the present analysis, which provides the two criteria  $D_k \leq 2.5 \times 10^{-3}$  and  $D_k \leq 2.5 \times 10^{-4}$ . The two corresponding accuracy limits are expressed in terms of number of points per wavelength, by  $\lambda_p/\Delta x$  and  $\lambda_a/\Delta x$ . These limits are given in Table 2 for the standard and the optimized filters. The optimized filters take into account short waves in a better way than the

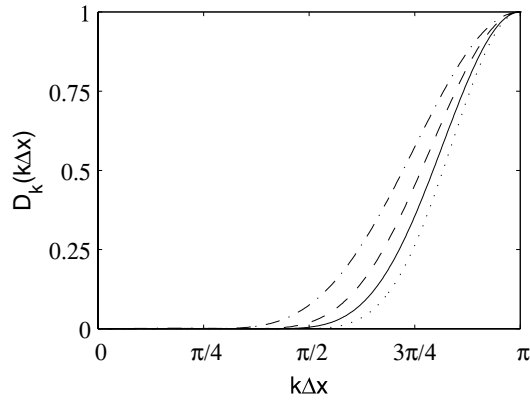


Fig. 3. Damping functions of the optimized selective filters: ---, SFo9p ( $N = 4$ ); —, SFo11p ( $N = 5$ ); ····, SFo13p ( $N = 6$ ) and -·-·- of the optimized filter proposed by Tam et al. [9] ( $N = 3$ ).

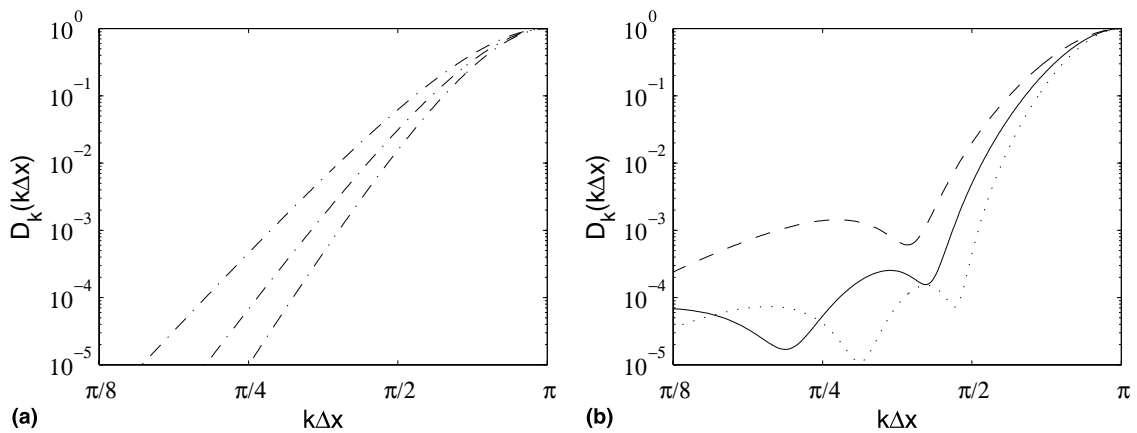


Fig. 4. Damping functions, in logarithmic scales, of: (a) -·-·- the three standard filters SFs9p, SFs11p and SFs13p; (b) the optimized filters --- SFo9p, — SFo11p and ···· SFo13p.

Table 2

Accuracy limits of the standard and optimized selective filters for  $N = 4, 5, 6$ ; and products by the number of points  $p = 2N + 1$  of the stencil

	$\lambda_p/\Delta x$	$\lambda_a/\Delta x$	$p\lambda_p/\Delta x$	$p\lambda_a/\Delta x$
SFs9p	6.38	8.67	57.4	78
SFs11p	5.4	6.96	59.4	76.6
SFs13p	4.82	5.99	62.7	77.9
SFo9p	4.7	15.81	42.3	142.3
SFo11p	4.17	6	45.9	66
SFo13p	3.74	4.08	48.6	53

For comparison, with the filter of Tam et al. [9] for  $N = 3$ :  $\lambda_p/\Delta x = 6$  and  $\lambda_a/\Delta x = 48.6$ .

standard ones. The products of the accuracy limits by the number of points  $2N + 1$  are also provided in Table 2 and present smaller values for the optimized filters. This demonstrates that the SFo11p and SFo13p filters are more efficient numerically.

#### 4. Runge–Kutta algorithms for time integration

We now consider the time integration using Runge–Kutta algorithms of the differential equation

$$\frac{\partial u}{\partial t} = F(u), \tag{4}$$

where the operator  $F$  is a function of  $u$ . Formulations of Runge–Kutta schemes have been proposed [14,25] to improve accuracy while reducing storage requirements. It is the case for the low-storage, explicit Runge–Kutta algorithms [23,26] using only two storage locations per variable. An explicit  $p$ -stage algorithm advances the solution of Eq. (4) from the  $n$ th to the  $(n + 1)$ th iterations as

$$\begin{aligned} u^0 &= u^n, \\ u^l &= u^n + \alpha_l \Delta t F(u^{l-1}) \quad \text{for } l = 1, \dots, p, \\ u^{n+1} &= u^p, \end{aligned}$$

where  $\alpha_l$  are the coefficients of the algorithm and  $\Delta t$  is the time step.

For  $F(u)$  linear, the algorithm is developed as

$$u^{n+1} = u^n + \sum_{j=1}^p \underbrace{\prod_{l=p-j+1}^p \alpha_l \Delta t^j}_{\gamma_j} \frac{\partial^j u^n}{\partial t^j}. \tag{5}$$

A  $p$ -stage algorithm of order  $p$  can be obtained by setting  $\gamma_j = 1/j!$  for  $l = 1, \dots, p$  to match the Taylor series of  $u(t_n + \Delta t)$ . The standard explicit four-stage Runge–Kutta algorithm RKs4s is defined by this way. It is of fourth order in linear, but only of second order in nonlinear as any scheme of this kind.

In the present work, explicit algorithms are constructed by optimizing their dispersion and dissipation properties following the idea of Hu et al. [13]. Assuming  $F(u)$  is linear and applying temporal Fourier transform to (5), the amplification factor of the algorithm is given by

$$G_{\text{RK}}(\omega \Delta t) = \frac{\hat{u}^{n+1}(\omega)}{\hat{u}^n(\omega)} = 1 + \sum_{j=1}^p \gamma_j (i\omega \Delta t)^j.$$

For comparison with the exact amplification factor  $e^{i\omega \Delta t}$ , it is written as  $|G_{\text{RK}}(\omega \Delta t)| e^{i\omega^* \Delta t}$ , where  $|G_{\text{RK}}|$  is the amplification rate and  $\omega^*$  is the effective angular frequency. For the angular frequency  $\omega$ , the amount of dissipation is then  $1 - |G_{\text{RK}}(\omega \Delta t)|$  and the difference in phase is  $\omega^* \Delta t - \omega \Delta t$ .

Two explicit five- and six-stage Runge–Kutta algorithms referred to as RKo5s and RKo6s, respectively, are built up by optimizing the dissipation and the dispersion errors up to the angular frequency  $\omega \Delta t = \pi/2$ . Both are of second order and are defined by coefficients  $\gamma_l$  minimizing the following error:

$$\int_{\ln(\pi/16)}^{\ln(\pi/2)} (1 - |G_{\text{RK}}(\omega \Delta t)|) d(\ln(\omega \Delta t)) + \int_{\ln(\pi/16)}^{\ln(\pi/2)} (|\omega^* \Delta t - \omega \Delta t|/\pi) d(\ln(\omega \Delta t)),$$

with these two conditions for the dissipation rate

$$\begin{cases} 1 - |G_{\text{RK}}| > 0, \\ \partial[\ln(1 - |G_{\text{RK}}|)]/\partial[\ln(\omega \Delta t)] \geq -5, \end{cases}$$

for  $0 \leq \omega \Delta t \leq \pi$ , as for the selective filters. The coefficients  $\gamma_l$  are provided in Appendix C.

The amplification rates and the differences in phase of the standard RKs4s and the optimized algorithms are plotted in Figs. 5(a) and (b), respectively. The optimized algorithms are both less dissipative and less dispersive than the standard RKs4s because their amplification rates are close to 1 and their differences in phase are close to 0 in a larger range of angular frequencies.

The stability of the algorithms, detected for  $|G_{\text{RK}}| < 1$ , appears higher for the optimized schemes. This is demonstrated by the stability limits reported in Table 3 and expressed in terms of number of iterations by  $T_s/\Delta t$ , where  $T_s$  is the period associated to the highest frequency ensuring stability for the time step  $\Delta t$ . The products of these limits by the number of stages are also shown in this table and they are similar for the three algorithms. Therefore, in the case of time steps only determined from stability, the computational costs are the same. The stability of the optimized algorithms must also be compared to the poor stability of the five- and six-stage algorithms proposed by Hu et al. [13].

The dissipation  $1 - |G_{\text{RK}}|$  and the phase error  $E_\omega(\omega\Delta t) = |\omega^*\Delta t - \omega\Delta t|/\pi$  of the Runge–Kutta algorithms are now represented in logarithmic scales in Fig. 6. Both optimized algorithms are less dissipative and dispersive than the standard RKs4s in the range  $\pi/8 \leq \omega\Delta t \leq \pi$ , RKo6s also being significantly more accurate than RKo5s. The improvement is spectacular for the dissipation with about one order of magnitude of difference between RKs4s and RKo5s, and between RKo5s and RKo6s.

Two accuracy limits are provided in Table 4. For dissipation, the criteria  $1 - |G_{\text{RK}}| \leq 5 \times 10^{-4}$  and  $1 - |G_{\text{RK}}| \leq 5 \times 10^{-5}$  are used to determine  $T_p^d/\Delta t$  and  $T_a^d/\Delta t$ . For the phase error, the criteria  $E_\omega \leq 5 \times 10^{-4}$  and  $E_\omega \leq 5 \times 10^{-5}$  are applied to evaluate  $T_p^\omega/\Delta t$  and  $T_a^\omega/\Delta t$ . The RKo5s algorithm improves the accuracy with respect to RKs4s both in dissipation and in phase, and in the same proportions. The RKo6s algorithm

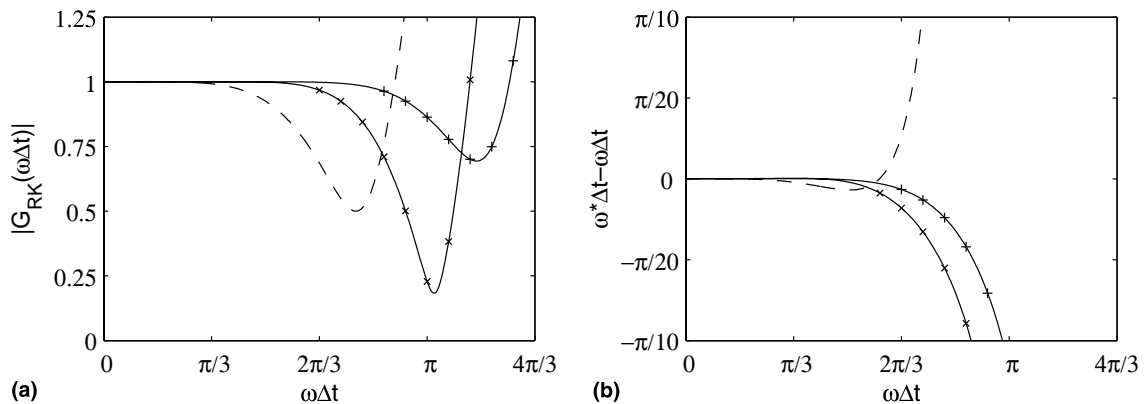


Fig. 5. (a) Amplification rate and (b) difference in phase of the Runge–Kutta schemes: ---, the standard RKs4s ( $p = 4$ ); —, the optimized schemes;  $\times$ , RKo5s ( $p = 5$ ) and  $+$ , RKo6s ( $p = 6$ ).

Table 3  
Stability limits of the standard and optimized Runge–Kutta algorithms, and products by the number of stages

	$T_s/\Delta t$	$pT_s/\Delta t$
RKs4s	2.22	8.9
RKo5s	1.76	8.8
RKo6s	1.59	9.5

For comparison, with the five- and six-stage optimized algorithms of Hu et al. [13]:  $T_s/\Delta t = 4.16$  and  $3.8$ , respectively.

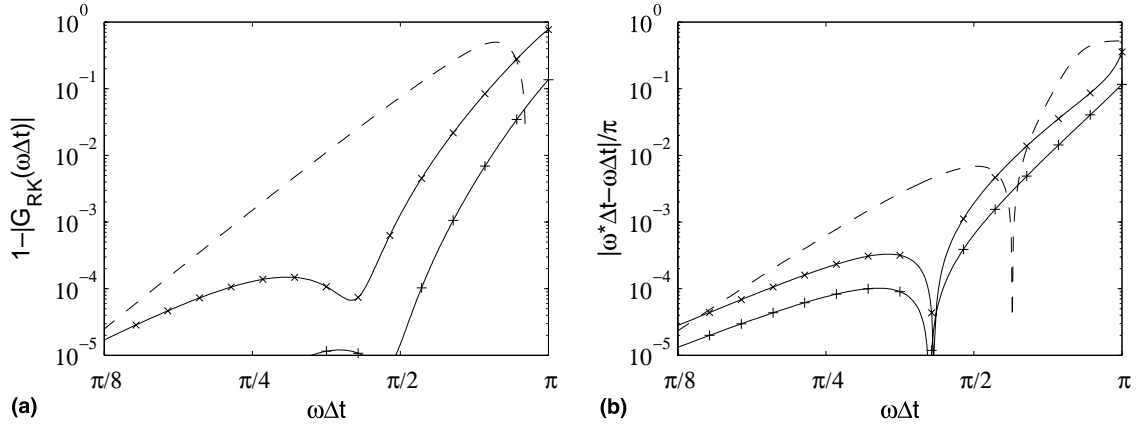


Fig. 6. (a) Dissipation and (b) dispersion error in logarithmic scales. See caption of Fig. 5 for details.

Table 4  
Accuracy limits in amplitude and in phase of the standard and optimized Runge–Kutta algorithms

	$T_p^d / \Delta t$	$T_a^d / \Delta t$	$T_p^\omega / \Delta t$	$T_a^\omega / \Delta t$
RKs4s	9.65	14.24	8.41	13.69
RKo5s	4.27	11.63	4.45	13.22
RKo6s	3.29	3.76	4.11	9.69

Table 5  
Accuracy limits multiplied by the number of stages for the standard and optimized Runge–Kutta algorithms

	$pT_p^d / \Delta t$	$pT_a^d / \Delta t$	$pT_p^\omega / \Delta t$	$pT_a^\omega / \Delta t$
RKs4s	38.6	57	33.6	54.8
RKo5s	21.4	58.2	22.2	66.1
RKo6s	19.8	22.6	24.6	58.1

still reduces the phase error, but its specific feature is given by its very low dissipation compared to the other algorithms.

Finally, numerical efficiencies are estimated by multiplying the accuracy limits, proportional to the number of iterations, by the number of stages, and they are displayed in Table 5. The optimized algorithms are clearly more efficient than the RKs4s. For the same computational cost, they provide more accurate results than the standard RKs4s algorithm.

### 5. Test filters

In the dynamic subgrid modelings used in Large Eddy Simulation, filterings of the resolved variables are involved to determine the magnitude of the subgrid terms. Application to variable  $u$  is written, as for the grid-to-grid oscillation filterings, as

$$u^f(x_0) = u(x_0) - D_u(x_0),$$

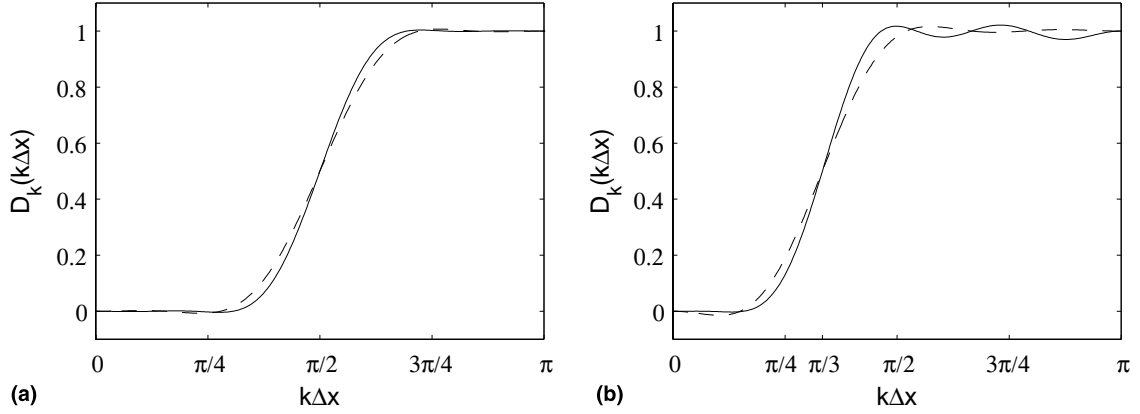


Fig. 7. Damping functions of the test filters: (a) --- TFo11p<sub>π/2</sub> (*N* = 5), and — TFo15p<sub>π/2</sub> (*N* = 7); (b) --- TFo11p<sub>π/3</sub> (*N* = 5) and — TFo15p<sub>π/3</sub> (*N* = 7).

with  $D_u(x_0)$  given by expression (2). Usually, the LES grid filter width is estimated as  $\Delta x$  and test filters with an effective width of  $2\Delta x$  or  $3\Delta x$  are used. These filters are constrained so that their damping functions (3) are such as  $D_k(k_c\Delta x) = 1/2$  for  $k_c\Delta x = \pi/2$  and  $k_c\Delta x = \pi/3$ , respectively.

To construct cut-off test filters, their coefficients  $d_j$  can be evaluated by vanishing the low-order terms [19] in the Taylor series of  $D_k(k\Delta x)$  for  $k\Delta x \rightarrow 0$ , and of  $1 - D_k(k\Delta x)$  for  $k\Delta x \rightarrow \pi$ . However, to obtain filters with better characteristics in the whole range of wavenumbers, using a minimization procedure in Fourier space is more interesting. In the present work, test filters with  $k_c\Delta x = \pi/2$  and  $k_c\Delta x = \pi/3$  are built up in this way. We impose  $D_k(0) = 0$ ,  $D_k(\pi) = 1$  and  $D_k(k_c\Delta x) = 1/2$ . For a sharp gradient near the cut-off wavenumber, we also set  $d_{2j} = 0$  and  $d_{3j} = 0$  ( $j \neq 0$ ), respectively, for the two kinds of filters. The other coefficients are optimized to minimize

$$\int_{\ln(\pi/16)}^{\ln(k_c\Delta x/\sqrt{2})} |D_k(k\Delta x)| d(\ln(k\Delta x)) + \int_{\ln(\sqrt{2}k_c\Delta x)}^{\ln(\pi)} |1 - D_k(k\Delta x)| d(\ln(k\Delta x)).$$

The proposed test filters, TFo11p<sub>π/2</sub>, TFo15p<sub>π/2</sub>, TFo11p<sub>π/3</sub> and TFo15p<sub>π/3</sub>, require 11 or 15 points, and their damping functions are displayed in Figs. 7(a) and (b). They appear to be selective enough to eliminate the wavenumbers such as  $k > k_c$  without significantly affecting the waves numbers with  $k < k_c$ . Their coefficients  $d_j$  are provided in Appendix D.

## 6. Test problems

### 6.1. Definition

Two basic problems are considered to illustrate the relative accuracy of the standard and the optimized schemes used for spatial derivation, grid-to-grid selective filtering and time integration. Both involve the long-range propagation of one-dimensional disturbances, allowing the observation of dispersion or dissipation errors. The convective wave equation

$$\frac{\partial u}{\partial t} + \frac{\partial u}{\partial x} = 0$$

is solved with a time step derived from the mesh spacing as  $\Delta t = \alpha\Delta x$ ,  $\alpha$  being the CFL number.

Initial disturbances at  $t = 0$  are defined as

$$u(x) = \sin\left(\frac{2\pi x}{a\Delta x}\right) \exp\left(-\ln(2)\left(\frac{x}{b\Delta x}\right)^2\right),$$

where  $a\Delta x$  is the dominant wavelength and  $b\Delta x$  the half-width of the Gaussian function. They are presented in Fig. 8. The parameters  $a$  and  $b$  are directly connected to the spectral contents of the disturbances, and we set  $a = 8$  and  $b = 3$  for problem I,  $a = 4$  and  $b = 9$  for problem II. The normalized spatial power spectral densities of the initial disturbances are thus displayed in Fig. 9.

Problem I is a typical test case to study propagation over a large distance. The initial perturbation is characterized by wavenumbers in the range  $0 < k\Delta x < \pi/2$  with a peak for  $k\Delta x = \pi/4$ , i.e., for eight points per wavelength. It is propagated over  $800\Delta x$  corresponding to 100 times the dominant wavelength, to emphasize the possible numerical errors. The motivation for problem II is to investigate the way the wavenumbers such as  $k\Delta x \simeq \pi/2$ , with about four points per wavelength, are calculated. These waves are often involved in the LES dynamic procedure to evaluate the modeling constants. The initial perturbation is propagated over a distance of  $200\Delta x$  corresponding to 50 times the wavelength.

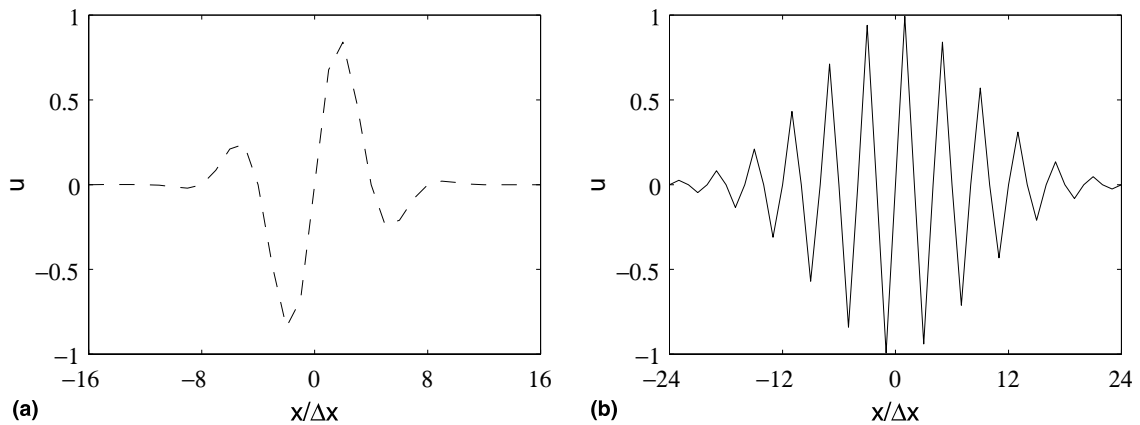


Fig. 8. Initial disturbances for: ---, problem I and — problem II.

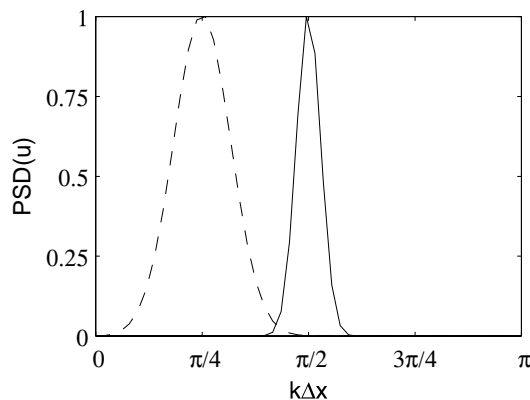


Fig. 9. Spectral contents of the initial disturbances for: ---, problem I and — problem II.

For the two problems, to quantify the agreement between the exact and the calculated solutions, the error rate  $e_{\text{num}}$  is evaluated as

$$e_{\text{num}} = \left( \frac{\sum (u_{\text{calc}} - u_{\text{exact}})^2}{\sum u_{\text{exact}}^2} \right)^{1/2}.$$

### 6.2. Problem I

First, problem I is solved using the different standard and optimized finite-difference schemes, no filtering, and the RKo6s algorithm with a time step small enough to introduce negligible errors since the CFL number is  $\alpha = 0.2$ . The results obtained with the standard schemes are presented in Fig. 10(a), and with the optimized schemes in Fig. 10(b). The solutions using the standard schemes all show more or less dispersion of the initial disturbance. The solution using the optimized FDo9p scheme is slightly distorted, whereas the solutions using the FDo11p and FDo13p schemes superpose fairly on the exact solution. The agreement with the exact solution is demonstrated by the values of the numerical errors reported in Table 6. The errors with the optimized schemes are at least two times lower than the errors with the standard schemes using the same number of points. It should also be noted that the FDo11p scheme is very well suited to this problem.

Second, problem I is solved using the different standard and optimized selective filters, the FDo13p scheme and the RKs6s algorithm with the same small time step as previously. Filtering is applied at every iteration with  $\sigma_d = 0.2$ . The results calculated with the standard filters are displayed in Fig. 11(a), with the

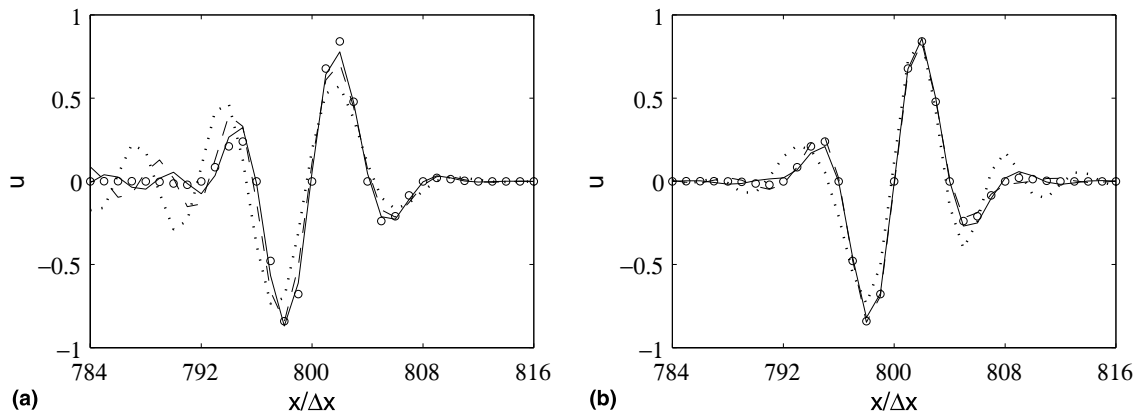


Fig. 10. Problem I.  $\circ$  exact solution; solutions using no filtering, RKo6s ( $\alpha = 0.2$ ) and: (a)  $\cdots$ , FDs9p;  $---$ , FDs11p and  $—$ , FDs13p; (b)  $\cdots$ , FDo9p;  $---$ , FDo11p and  $—$  FDo13p.

Table 6

Problem I. Errors  $e_{\text{num}}$  using the standard and the optimized finite-difference schemes, no filtering and the RKo6s algorithm ( $\alpha = 0.2$ )

FDs9p	0.630
FDs11p	0.307
FDs13p	0.141
FDo9p	0.329
FDo11p	0.052
FDo13p	0.065

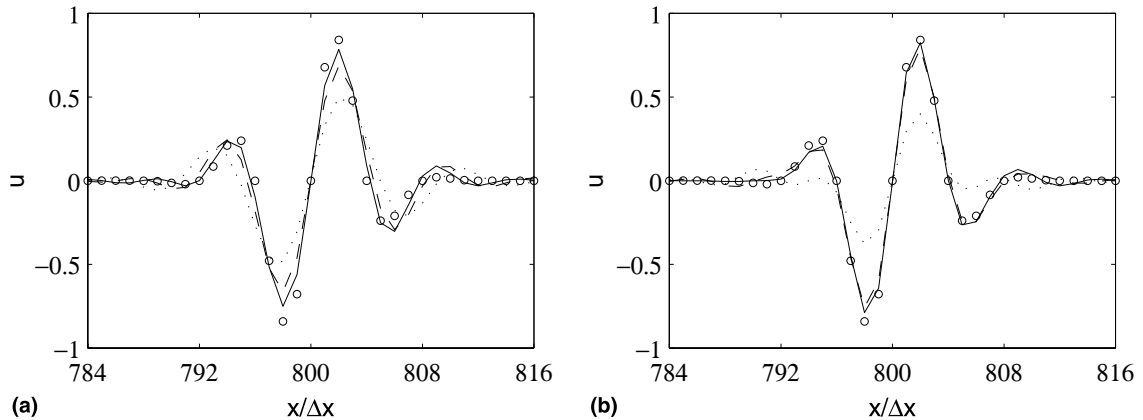


Fig. 11. Problem I.  $\circ$  exact solution; solutions using FDo13p, RKo6s ( $\alpha = 0.2$ ) and: (a)  $\cdots$ , SFs9p;  $---$ , SFs11p and  $—$ , SFs13p; (b)  $\cdots$ , SFo9p;  $---$  SFo11p and  $—$  SFo13p ( $\sigma_d = 0.2$ ).

optimized filters in Fig. 11(b), and they are compared to the exact solution. The solutions using the standard filters show dissipation of the initial perturbation, even for the SFs13p filter of order 12. The solution with the SFo9p filter is significantly dissipated, but the ones with the optimized SFo11p and SFo13p filters are not. This is supported by the values of  $e_{\text{num}}$  in Table 7. Except for the SFo9p filter, using the optimized selective filters instead of the standard ones remarkably decreases the dissipation of the disturbances involved in this problem. Besides numerical errors with the SFo13p filter can be mainly attributed to the spatial derivation.

Third, problem I is solved using the FDo13p scheme, the SFo13p filter and the standard or optimized explicit Runge–Kutta algorithms, with CFL numbers of  $\alpha = 0.2$ ,  $\alpha = 0.5$  and  $\alpha = 1$ . The solutions for  $\alpha = 0.5$  and for  $\alpha = 1$  are presented in Figs. 12(a) and (b), and the errors  $e_{\text{num}}$  are reported in Table 8 for the three CFL numbers. For  $\alpha = 0.2$ , the three algorithms provide very good results, but for  $\alpha = 0.5$  and  $\alpha = 1$ , the RKo6s algorithm is much more accurate than the two others. This is spectacularly visible for  $\alpha = 1$ : solutions are distorted and dissipated, highly with the RKs4s algorithm and slightly with the RKo5s one, whereas the solution found with the RKo6s algorithm is in agreement with the exact solution.

### 6.3. Problem II

Problem II is solved using the RKo6s algorithm with  $\alpha = 0.8$  and three finite-difference scheme/selective filter combinations: FDo9p and SFo9p, FDo11p and SFo11p, and FDo13p and SFo13p. The solutions obtained with the last two combinations are shown in Fig. 13. The wave packet is dispersed and dissipated using the 11-point methods, but it is well calculated using the 13-point methods. In the latter case, the

Table 7

Problem I. Errors  $e_{\text{num}}$  using the standard and the optimized selective filtering, FDo13p and RKo6s ( $\sigma_d = 0.2$ ,  $\alpha = 0.2$ )

SFs9p	0.533
SFs11p	0.303
SFs13p	0.168
SFo9p	0.580
SFo11p	0.114
SFo13p	0.077

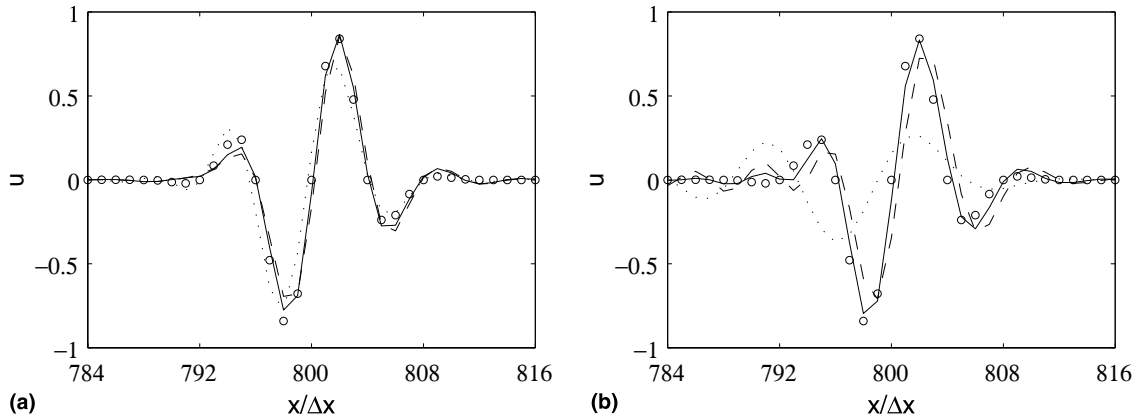


Fig. 12. Problem I.  $\circ$  exact solution; solutions using FDo13p, SFo13p ( $\sigma_d = 0.2$ ) and:  $\cdots$ , RKs4s;  $---$ , RKo5s;  $—$ , RKo6s; (a) for  $\alpha = 0.5$  and (b) for  $\alpha = 1$ .

Table 8

Problem I. Errors  $e_{\text{num}}$  using the RK schemes for different CFL numbers, the FDo13p and SFo13p schemes ( $\sigma_d = 0.2$ )

	$\alpha = 0.2$	$\alpha = 0.5$	$\alpha = 1$
RKs4s	0.070	0.269	0.884
RKo5s	0.086	0.229	0.528
RKo6s	0.077	0.122	0.200

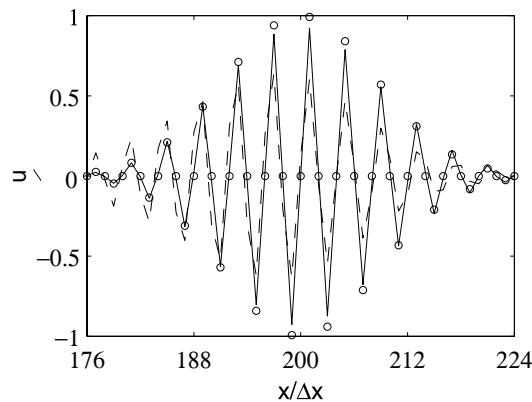


Fig. 13. Problem II.  $\circ$  exact solution; solutions using RKo6s ( $\alpha = 0.8$ ) with:  $---$  FDo11p and SFo11p,  $—$  FDo13p and SFo13p, ( $\sigma_d = 0.2$ ).

Table 9

Problem II. Errors  $e_{\text{num}}$  using optimized finite-difference schemes and selective filters with the RKo6s algorithm ( $\sigma_d = 0.2$ ,  $\alpha = 0.8$ )

FDo9p + SFo9p	0.905
FDo11p + SFo11p	0.488
FDo13p + SFo13p	0.077

computed solution is in phase with the exact one and is only very slightly dissipated. The errors  $e_{\text{num}}$  given in Table 9 support these observations and also show that the 9-point methods are not accurate enough to resolve this problem involving wavenumbers with  $k\Delta x \simeq \pi/2$ .

## 7. Applications

In this section, some remarks are made about the practical applications of the present optimized schemes. Two issues dealing with the spatial discretization schemes are discussed: first the way they can be connected with boundary conditions and second, the effects of grid non-uniformity on their properties. Examples of Large Eddy Simulations of turbulent flows using the present schemes are also reported.

### 7.1. Connection with boundary conditions

At the edge of the computational domain, boundary conditions are necessary to impose for instance free-field or wall conditions. They can be implemented using non-centered stencils with the same size as the centered stencil used for the interior points. This approach was particularly followed by Tam et al. [2,27] who provided both centered and backward DRP schemes with 7-point stencils. A common practice is, however, to use stencils with smaller size near the boundaries. This is usually done to keep centered schemes, for stability concern.

In our first simulations with the present spatial discretization schemes, the second method was used for the boundary conditions. The size of the stencil is decreased progressively, from 9, 11 or 13 points in the interior domain to 3 or 5 points at the boundary. As an example, the standard second-order schemes are used to take into account wall boundaries in simulations of cavity flows [28]. For non-reflecting boundaries, the standard fourth-order schemes are implemented as illustrated in Fig. 14. In this case, the equations governing the acoustic far-field [29,30] are solved in three rows of points using standard 5-point stencil schemes for the  $y$ -derivatives. The connection with the optimized 11-point stencil is performed, thanks to the intermediary use of standard or optimized schemes with 7- and 9-point stencils.

### 7.2. Properties for a non-uniform grid

The standard high-order and optimized schemes presented in this paper are based on a uniformly spaced computational grid. They are, however, applied in most numerical simulations for non-uniform grids, where grid stretching is used to adapt the mesh size to the different length scales to be calculated. This results in discretization errors which can be significant for high grid non-uniformity and which are usually

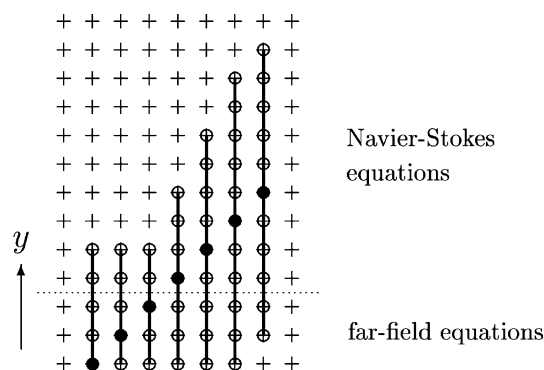


Fig. 14. An example of numerical implementation combining the 11-point stencil difference scheme with far-field boundary conditions applied in three rows of points. The  $y$ -derivatives at points ● are evaluated using points ○.

minimized using small stretching rates. For the optimized schemes, one particular question raised by grid stretching is about the damage caused to their dispersion and dissipation properties. One can also wonder whether these schemes remain more accurate than the standard ones for non-uniform grids. These points are here investigated for the spatial derivation on a non-uniform grid  $x$  in which the mesh spacing is stretched by a ratio  $r$ , yielding  $x_{j+1} = x_j + \Delta x r^{(j-1)}$ . Note that a quite similar study could be done for the selective filtering.

The spatial derivative  $\partial u / \partial x$  is classically evaluated as

$$\frac{\partial u}{\partial x} = \frac{\partial \xi}{\partial x} \frac{\partial u}{\partial \xi} = \frac{1}{\partial x / \partial \xi} \frac{\partial u}{\partial \xi},$$

where  $\xi$  is an arbitrary uniform grid. At the  $m$ th grid point, using a central  $2N + 1$  point stencil finite-difference scheme, it provides

$$\frac{\partial u}{\partial x}(x_m) = \frac{1}{\Delta x} \sum_{j=-N}^N a_j u_{m+j}, \quad \text{with } \tilde{\Delta x} = \sum_{j=-N}^N a_j x_{m+j}. \quad (6)$$

The wavenumber  $k^*$  estimated by the derivative on the non-uniform grid is then obtained by applying spatial Fourier transform to (6), which gives

$$k^* \Delta = -i \frac{\Delta}{\Delta x} \sum_{j=-N}^N a_j \exp(ik(x_{m+j} - x_m)),$$

where  $\Delta = (x_{m+1} - x_{m-1})/2$  is the local mesh size.

To discuss the effects of grid stretching, the difference between the exact and the effective wavenumbers  $k$  and  $k^*$  is calculated for the standard and the optimized 11-point stencil schemes FDs11p and FDo11p, in the case of stretching rates of  $r = 2\%$  and  $8\%$ . Fig. 15 presents the dispersion error estimated from the real part of  $k^*$ , whereas Fig. 16 displays the imaginary part of  $k^*$ , responsible for the error in amplitude. For the stretching rate  $r = 2\%$ , the numerical errors on the wave numbers in the range  $\pi/4 \leq k\Delta \leq \pi/2$  are significantly reduced using FDo11p instead of FDs11p. However, for the rate of  $r = 8\%$ , the errors generated by the two schemes do not appreciably differ. This shows that the optimized schemes developed in the present paper keep better accuracy than the standard ones for small stretching rates, typically up to about  $r = 5\%$ . They can therefore be recommended as long as the grid stretching is reasonable, as in our simulations [28,31], where stretching rates of only 2% or 3% are used.

### 7.3. Large Eddy Simulations of turbulent flows

The schemes developed in this paper have recently been used to solve the full three-dimensional Navier–Stokes equations. Subsonic flows past rectangular open cavities and Mach number  $M = 0.9$ , circular jets have been successfully simulated using the RKo6s algorithm for the time integration and, respectively, the FDo11p and SFo11p, and the FDo13p and SFo13p schemes for the spatial discretization. Both flow configurations were at Reynolds numbers much higher than affordable by Direct Numerical Simulation and have therefore been computed by Large Eddy Simulation. The Reynolds numbers based on the cavity depth and on the jet nozzle diameter were indeed  $4 \times 10^4$  and  $4 \times 10^5$ . At such values, turbulence display a great disparity of length scales as illustrated by the jet vorticity field represented in Fig. 17. Using the optimized

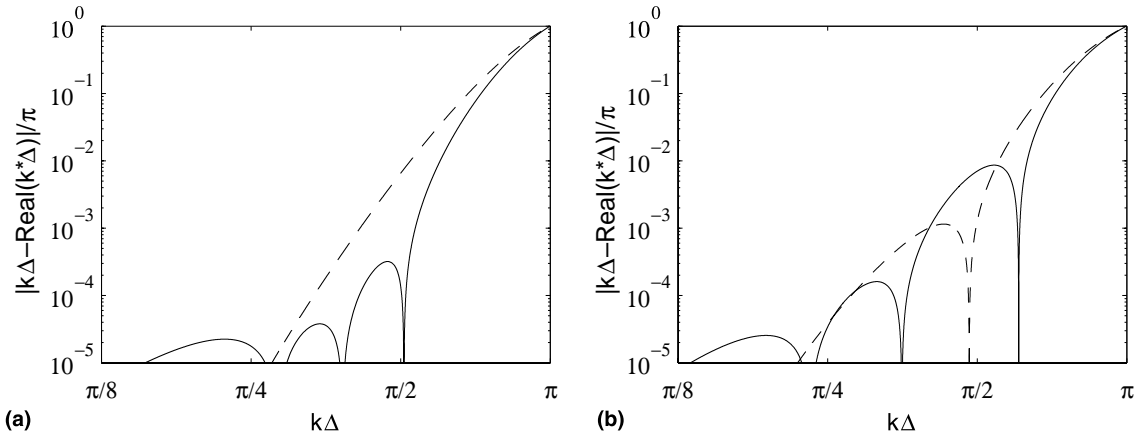


Fig. 15. Dispersion errors using — FD011p and --- FDs11p for non-uniform grids with spacing ratios of: (a)  $r = 2\%$  and (b)  $r = 8\%$ .

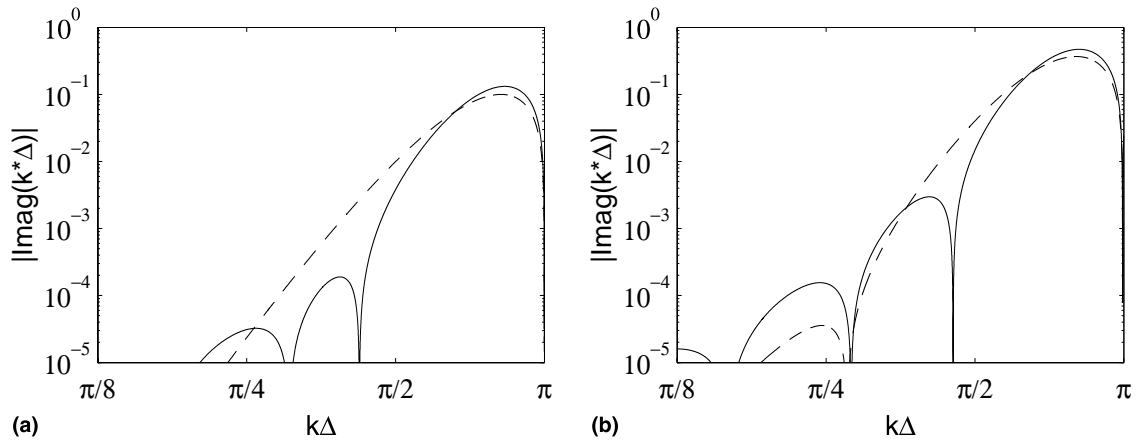


Fig. 16. Imaginary part of the effective wavenumbers calculated using — FD011p and --- FDs11p for non-uniform grids with spacing ratios of: (a)  $r = 2\%$  and (b)  $r = 8\%$ .

schemes, one can at least consider that all the scales discretized by more than four grid points are accurately resolved. For the detailed description of the simulation results and the comparisons with measurements, the reader is referred to [28,31].

The use of the optimized schemes appears also especially relevant for the Large Eddy Simulation methodology. First, they permit to define a sharp, spectral-like cut-off of the turbulent scales at the filtering wavenumber around  $k_c^{sf} = \pi/(2\Delta x)$  for four point per wavelength. Second, they allow to ensure that the shorter resolved scales, involved in the dynamic procedures of subgrid modeling, are not distorted by the discretization, and thus that the model coefficients are not calculated from numerical artifacts. This was the primary motivation for developing new explicit schemes, see for instance, the application of the dynamic Smagorinsky modeling to the circular jet in [32]. A third point can also be reported about the possible use of the selective filtering for taking into account the dissipative effects of the subgrid scales instead of an eddy-viscosity model as in [31–33]. In this way, the turbulent energy is dissipated only through

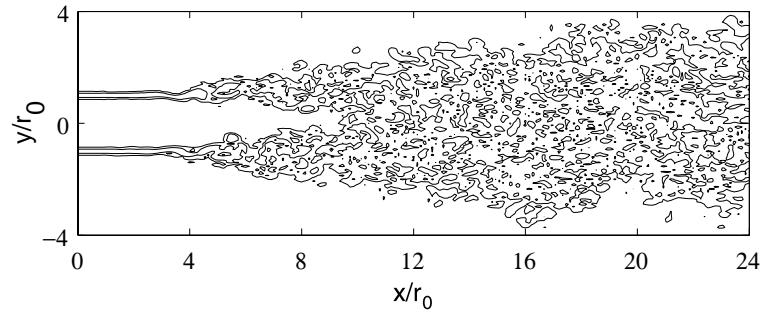


Fig. 17. Spatial evolution of a circular jet at Mach 0.9 and Reynolds number  $4 \times 10^5$ . View of the two vorticity-norm contours associated with the magnitudes of  $3.2 \times 10^4$  and  $9.6 \times 10^4 \text{ s}^{-1}$  in the  $x$ - $y$  plane at  $z = 0$ .

the short scales characterized by  $k \geq k_c^{sf}$ . This approach may be particularly interesting at high Reynolds numbers where the larger scales must be dissipation-free.

## 8. Conclusion

A family of explicit methods including finite-difference schemes for spatial derivation, low-storage Runge–Kutta algorithms for time integration, selective filters for eliminating grid-to-grid oscillations and test filters is proposed. The characteristics of these methods are optimized by minimizing the numerical errors for the same range of wavenumbers, so that they can be associated to form algorithms with spectral-like resolution. This is of importance with the aim of performing with confidence 3-D computations, where dependence of results on numeric schemes can hardly be investigated through parametric studies. Analysis of dispersion and dissipation properties, evaluation of accuracy limits, and resolution of test problems demonstrate the higher precision of the optimized methods for short waves with respect to the standard explicit ones, even for slowly non-uniform grids with stretching rates of few per cent. Numerical efficiency is also discussed and it is shown that for an identical computational cost, optimized methods provide higher accurate results. Considering this, the algorithm using the 11-point stencil finite-difference scheme and selective filter, and the six-stage Runge–Kutta scheme, showing stability up to a CFL number  $\alpha = 1.98$ , appears especially appropriate. Finally, the schemes developed in this paper can be clearly used both for long-range propagation problems and for simulating turbulent flows, as shown by recent applications using Large Eddy Simulations.

## Appendix A. Finite-difference schemes

Coefficients of the standard high-order schemes using 9-, 11- and 13-point stencils ( $a_0 = 0$ ,  $a_{-j} = -a_j$ ):

	FDs9p	FDs11p	FDs13p
$a_1$	4/5	5/6	6/7
$a_2$	-1/5	-5/21	-15/56
$a_3$	4/105	5/84	5/63
$a_4$	-1/280	-5/504	-1/56
$a_5$		1/1260	3/1155
$a_6$			-1/5544

Coefficients of the optimized schemes using 9-, 11- and 13-point stencils ( $a_0 = 0$ ,  $a_{-j} = -a_j$ ):

	FD09p	FD011p	FD013p
$a_1$	0.841570125482	0.872756993962	0.907646591371
$a_2$	-0.244678631765	-0.286511173973	-0.337048393268
$a_3$	0.059463584768	0.090320001280	0.133442885327
$a_4$	-0.007650904064	-0.020779405824	-0.045246480208
$a_5$		0.002484594688	0.011169294114
$a_6$			-0.001456501759

### Appendix B. Selective filters

Coefficients of the standard high-order filters using 9-, 11- and 13-point stencils ( $d_{-j} = d_j$ ):

	SFs9p	SFs11p	SFs13p
$d_0$	35/128	63/256	231/1024
$d_1$	-7/32	-105/512	-99/512
$d_2$	7/64	15/128	495/4096
$d_3$	-1/32	-45/1024	-55/1024
$d_4$	1/256	5/512	33/2048
$d_5$		-1/1024	-3/1024
$d_6$			1/4096

Coefficients of the optimized selective filters using 9-, 11- and 13-point stencils ( $d_{-j} = d_j$ ):

	SFo9p	SFo11p	SFo13p
$d_0$	0.243527493120	0.215044884112	0.190899511506
$d_1$	-0.204788880640	-0.187772883589	-0.171503832236
$d_2$	0.120007591680	0.123755948787	0.123632891797
$d_3$	-0.045211119360	-0.059227575576	-0.069975429105
$d_4$	0.008228661760	0.018721609157	0.029662754736
$d_5$		-0.002999540835	-0.008520738659
$d_6$			0.001254597714

### Appendix C. Runge–Kutta algorithms

Coefficients of the 4-stage 4th-order algorithm and of the 5- and 6-stage optimized algorithms:

	RKs4s	RKo5s	RKo6s
$\gamma_1$	1	1	1
$\gamma_2$	1/2	1/2	1/2
$\gamma_3$	1/6	0.165250353664	0.165919771368
$\gamma_4$	1/24	0.039372585984	0.040919732041
$\gamma_5$		0.007149096448	0.007555704391
$\gamma_6$			0.000891421261

## Appendix D. Test filters

Coefficients of the optimized test filters with  $k_c \Delta x = \pi/2$  using 11- and 15-point stencils ( $d_{-j} = d_j$ ):

	TFo11p $_{\pi/2}$	TFo15p $_{\pi/2}$
$d_0$	1/2	1/2
$d_1$	-0.30399520	-0.30834723
$d_2$	0	0
$d_3$	0.06880899	0.07876835
$d_4$	0	0
$d_5$	-0.01481379	-0.02617123
$d_6$		0
$d_7$		0.00575011

Coefficients of the optimized test filters with  $k_c \Delta x = \pi/3$  using 11- and 15-point stencils ( $d_{-j} = d_j$ ):

	TFo11p $_{\pi/3}$	TFo15p $_{\pi/3}$
$d_0$	2/3	2/3
$d_1$	-0.26775782	-0.26598093
$d_2$	-0.12016956	-0.12936060
$d_3$	0	0
$d_4$	0.03683622	0.04602726
$d_5$	0.01775782	0.03212998
$d_6$		0
$d_7$		-0.01614906

## References

- [1] C.K.W. Tam, Computational aeroacoustics: issues and methods, *AIAA J.* 33 (10) (1995) 1788.
- [2] C.K.W. Tam, J.C. Webb, Dispersion-relation-preserving finite difference schemes for computational acoustics, *J. Comput. Phys.* 107 (1993) 262.
- [3] S.K. Lele, Compact finite difference schemes with spectral-like resolution, *J. Comput. Phys.* 103 (1) (1992) 16.
- [4] Z. Haras, S. Ta'asan, Finite difference schemes for long-time integration, *J. Comput. Phys.* 114 (1994) 265.
- [5] J.W. Kim, D.J. Lee, Optimized compact schemes with maximum resolution, *AIAA J.* 34 (5) (1996) 887.
- [6] K. Mahesh, A family of high order finite difference schemes with good spectral resolution, *J. Comput. Phys.* 145 (1998) 332.
- [7] R. Hixon, Prefactored small-stencil compact schemes, *J. Comput. Phys.* 165 (2) (2000) 522.
- [8] D.P. Lockard, K.S. Brentner, H.L. Atkins, High-accuracy algorithms for computational aeroacoustics, *AIAA J.* 33 (2) (1995) 246.
- [9] C.K.W. Tam, J.C. Webb, Z. Dong, A study of the short wave components in computational acoustics, *J. Comput. Ac.* 1 (1) (1993) 1.
- [10] C.K.W. Tam, H. Shen, Direct computation of nonlinear acoustic pulses using high order finite difference schemes, *AIAA Paper* 93-4325, 1993.
- [11] M.R. Visbal, D.V. Gaitonde, High-order-accurate methods for complex unsteady subsonic flows, *AIAA J.* 37 (10) (1999) 1231.
- [12] D.W. Zingg, H. Lomax, H. Jurgens, High-accuracy finite-difference schemes for linear wave propagation, *SIAM J. Sci. Comput.* 17 (2) (1996) 328.
- [13] F.Q. Hu, M.Y. Hussaini, J.L. Mantney, Low-dissipation and low-dispersion Runge–Kutta schemes for computational acoustics, *J. Comput. Phys.* 124 (1996) 177.
- [14] D. Stanescu, W.G. Habashi, 2N-storage low dissipation and dispersion Runge–Kutta schemes for computational acoustics, *J. Comput. Phys.* 143 (1998) 674.
- [15] R. Hixon, E. Turkel, Compact implicit MacCormack-type schemes with high accuracy, *J. Comput. Phys.* 158 (1) (2000) 51.

- [16] C. Bogey, C. Bailly, D. Juvé, Numerical simulation of the sound generated by vortex pairing in a mixing layer, *AIAA J.* 38 (12) (2000) 2210.
- [17] C. Bogey, C. Bailly, D. Juvé, Noise investigation of a high subsonic, moderate Reynolds number jet using a compressible LES, *Theoret. Comput. Fluid Dyn.* 16 (4) (2003) 273.
- [18] M. Lesieur, O. Métais, New trends in large-Eddy simulations of turbulence, *Annu. Rev. Fluid Mech.* 28 (1996) 45.
- [19] O.V. Vasilyev, T.S. Lund, P. Moin, A general class of commutative filters for LES in complex geometry, *J. Comput. Phys.* 146 (1998) 82.
- [20] M. Germano, U. Piomelli, P. Moin, W.H. Cabot, A dynamic subgrid-scale Eddy viscosity model, *Phys. Fluids A* 3 (7) (1991) 1760.
- [21] S. Ghosal, An analysis of numerical errors in Large-Eddy Simulations of turbulence, *J. Comput. Phys.* 125 (1996) 187.
- [22] A.G. Kravchenko, P. Moin, On the effect of numerical errors in Large Eddy Simulations of turbulent flows, *J. Comput. Phys.* 131 (1997) 310.
- [23] A. Jameson, W. Schmidt, E. Turkel, Numerical solution of the Euler equations by finite volume methods using Runge–Kutta time stepping schemes, *AIAA Paper* 81-1259, 1981.
- [24] C.A. Kennedy, M.H. Carpenter, Several new numerical methods for compressible shear-layer simulations, *Appl. Numer. Math.* 14 (2) (1994) 397.
- [25] M.H. Carpenter, C.A. Kennedy, A fourth-order  $2N$  storage Runge–Kutta scheme, *NASA TM-109112*, 1994.
- [26] J.H. Williamson, Low-storage Runge–Kutta schemes, *J. Comput. Phys.* 35 (1980) 48.
- [27] C.K.W. Tam, Z. Dong, Wall boundary conditions for high-order finite-difference schemes in computational aeroacoustics, *Theoret. Comput. Fluid Dyn.* 6 (1994) 303.
- [28] X. Gloerfelt, C. Bogey, C. Bailly, D. Juvé, Aerodynamic noise induced by laminar and turbulent boundary layers over rectangular cavities, *AIAA Paper* 2002-2476, 2002 (see also *AIAA Paper* 2003-3234, 2003).
- [29] C.K.W. Tam, Z. Dong, Radiation and outflow boundary conditions for direct computation of acoustic and flow disturbances in a nonuniform mean flow, *J. Comput. Ac.* 4 (2) (1996) 175.
- [30] C. Bogey, C. Bailly, Three-dimensional non reflective boundary conditions for acoustic simulations: far-field formulation and validation test cases, *Acta Acoustica* 88 (4) (2002) 463.
- [31] C. Bogey, C. Bailly, Direct computation of the sound radiated by a high Reynolds number, subsonic round jet, in: *CEAS Workshop From CFD to CAA*, Athens, Greece, November 7–8, 2002 (see also *AIAA Paper* 2003-3170, 2003).
- [32] C. Bogey, C. Bailly, LES of a high Reynolds, high subsonic jet: effects of the subgrid modellings on flow and noise, *AIAA Paper* 2003-3557, 2003.
- [33] M.R. Visbal, D.P. Rizzetta, Large-Eddy Simulation on curvilinear grids using compact differencing and filtering schemes, *J. Fluid Engrg.* 124 (2002) 836.